

# Learning Weather Models from Data with WSINDy

Seth Minor<sup>1</sup>, Daniel A. Messenger<sup>2</sup>, Vanja Dukic<sup>1\*</sup>, and David M. Bortz<sup>1\*</sup>

<sup>1</sup>Department of Applied Mathematics, University of Colorado, Boulder, CO 80309-0526 USA

<sup>2</sup>Theoretical Division, Los Alamos National Laboratory, Los Alamos, NM 87545 USA

## Key Points:

- We review the Weak form Sparse Identification for Nonlinear Dynamics (WSINDy) algorithm and illustrate how it can be adapted to learn interpretable mathematical models from noisy weather data.
- We apply WSINDy to three simulated datasets exhibiting phenomena of interest to geophysics researchers, including: (1) an equivalent barotropic turbulence model, (2) the Shallow Water Equations on a sphere, and (3) a stably-stratified atmospheric boundary layer model.
- We also apply WSINDy to assimilated global-scale weather data from the European Center for Medium-Range Weather Forecasts v5 Reanalysis.

---

\*Joint senior authors

Corresponding author: Seth Minor, [seth.minor@colorado.edu](mailto:seth.minor@colorado.edu)

Corresponding author: David Bortz, [david.bortz@colorado.edu](mailto:david.bortz@colorado.edu)

**Abstract**

The multiscale and turbulent nature of Earth’s atmosphere has historically rendered accurate weather modeling a hard problem. Recently, there has been an explosion of interest surrounding data-driven approaches to weather modeling, which in many cases show improved forecasting accuracy and computational efficiency when compared to traditional methods. However, many of the current data-driven approaches employ highly parameterized neural networks, often resulting in uninterpretable models and limited gains in scientific understanding. In this work, we address the interpretability problem by explicitly discovering partial differential equations governing various weather phenomena, identifying symbolic mathematical models with direct physical interpretations. The purpose of this paper is to demonstrate that, in particular, the Weak form Sparse Identification of Nonlinear Dynamics (WSINDy) algorithm can learn effective weather models from both simulated and assimilated data. Our approach adapts the standard WSINDy algorithm to work with high-dimensional fluid data of arbitrary spatial dimension. Moreover, we develop an approach for handling terms that are not integrable-by-parts, such as advection operators.

## 1 Introduction and Previous Work

Since its modern inception in the pioneering computational work of Charney, Fjörtoft, and Von Neumann (see Charney et al. (1950)), numerical weather prediction (NWP) has proven to present formidable mathematical challenges. In particular, many dynamic models of weather phenomena exhibit multiscale and turbulent features which have been known since the seminal work of Lorenz (1963) to lead to a sensitive dependence on initial conditions. As a consequence, the uncertainties present in a set of initial observations grow exponentially in time under these models, bounding the predictive power of most numerical weather forecasts to medium-range time scales ( $\leq 14$  days). This chaotic behavior is exacerbated by the computational reality that simulations of the relevant physics can only capture a finite range of scales, so that the physical influence of unresolved scales is either ignored or approximated by subgrid closure models.

In recent years, there has been an explosion of interest surrounding data-driven approaches to weather modeling (see, e.g., Rasp et al. (2024) and Karlbauer et al. (2024) for a discussion and recent benchmarks). In contrast to traditional NWP, which relies on numerical simulations of physics-based weather models, these novel data-driven approaches learn effective weather models directly from empirical data. A common theme of recent work in this area is the use of highly parameterized neural networks trained to predict future weather conditions using one of two modi operandi: (1) learn an effective model from the empirical data alone (without reference to external knowledge of the dynamics), or (2) incorporate physical knowledge to learn a model in a *hybrid* fashion (e.g., penalizing potential models that violate known physics). State-of-the-art examples in each of these two categories are, respectively, GraphCast (Lam et al., 2023), which uses graph neural networks to predict and relate weather dynamics on a range of length scales, and NeuralGCM (Kochkov et al., 2024), which uses a hybrid neural network architecture to represent parameterized physical processes included within an explicit base model. While such models achieve both (1) significant computational speedups (often by orders of magnitude) and (2) improved accuracy in forecasting over traditional methods (Rasp et al., 2024), the large number of parameters renders such models almost completely uninterpretable. For example, GraphCast has roughly  $\sim 36.7$  million parameters (Lam et al., 2023).

A separate thread of research seeks to discover sparse, data-driven weather models in a physically interpretable symbolic form, such as the effective governing partial differential equations (PDEs). Some recent approaches, e.g., Zanna and Bolton (2020), use physical data to learn explicit subgrid closure models, which are then appended onto classical PDEs to improve their accuracy when modeling real-world data. However, physical data can also be used to estimate the equations of motion in their entirety. A popular framework for learning PDEs from data is sparse dictionary learning, as used in, e.g., the Sparse Identification of Nonlinear Dynamics (SINDy) algorithm (Brunton et al., 2016). SINDy attempts to fit functions from a library of candidate terms to an evolution operator, while also using a regularized loss function to enforce a parsimonious solution with a relatively small number of terms. Unfortunately, the naïve SINDy algorithm is not robust to observational noise, potentially limiting the value of the approach in weather modeling contexts. However, recent advancements in data-driven model discovery, such as the development of Galerkin methods such as the Weak SINDy (WSINDy) algorithm (Messenger & Bortz, 2021) (see also, e.g., Reinbold et al. (2021) and Gurevich et al. (2024)), have substantially increased robustness to noise by representing and in turn learning the relevant dynamics in their weak form. In this formulation, the data are integrated against localized test functions which implicitly allow for both the extraction of signal-dominated modes and the imposition of a set of particular length and time scales.

The purpose of this paper is to demonstrate that WSINDy is a powerful tool for interpretable, data-driven geophysical modeling. We adapt WSINDy to the task of data-driven weather modeling, illustrating the discovery of effective PDE models from both simulated and assimilated weather data spanning several common meteorological regimes. We organize the paper as follows. In Section 2, we introduce the notational conventions used throughout (§2.1) before reviewing select background material related to mathematical weather modeling (§2.2), our implementation of the WSINDy algorithm (§2.3), and the performance metrics (§2.4) used to assess the quality of our results, commenting on cases of corrupted data in §2.5. We then present and discuss our model discovery results in Section 3, detailing our choice of hyperparameters (§3.1) used to obtain results on simulated (§3.2) and assimilated (§3.4) datasets. Finally, in Section 4, we conclude with a brief summary of the paper and some reflections on natural extensions of this work. Supplementary information about the datasets used to produce these results is given in the Appendix.

## 2 Methods and Background Material

Here, we provide a brief overview of the mathematical content we primarily draw upon in applying weak form model discovery to weather data. For a review of traditional PDE weather models, interested readers are directed towards the review given in White (2003). For a more complete discussion of weak form model discovery applied to spatiotemporal systems, readers are directed towards the recent SIAM News article (Messenger, Tran, et al., 2024b), its companion review article (Messenger, Tran, et al., 2024a), and the original WSINDy paper (Messenger & Bortz, 2021).

### 2.1 Notation and Conventions

In this paper, we consider  $(n + 1)$ -dimensional dynamics on bounded spatiotemporal domains  $(\mathbf{x}, t) \in \mathcal{X} \times [0, T]$ , where  $\mathcal{X} \subset \mathbb{R}^n$ . When referencing planetary scale weather data (as in Section 3.4), we use a geographic coordinate system in which  $\varphi \in [0, 2\pi)$  is the longitude,  $\theta \in [-\pi/2, \pi/2]$  is the latitude, and  $r \geq 0$  is the altitude. For such geographic coordinates, we use the symbols  $u$ ,  $v$ , and  $w$  to denote the zonal (east-west), meridional (north-south), and radial components of the wind velocity  $\mathbf{v} = (u, v, w)^T$ . We denote the horizontal surface velocity as  $\mathbf{u} = (u, v)^T$  and the scalar vorticity as  $\zeta = \nabla \times \mathbf{u}$ . When necessary, we approximate the rotation rate of Earth as  $\Omega = |\mathbf{\Omega}| \approx 7.2921 \cdot 10^{-5}$  (rads/s), where  $\mathbf{\Omega}$  is the planetary angular velocity vector. The Coriolis force induced by a reference frame rotating with the Earth is given by  $\mathbf{f} = 2(\mathbf{\Omega} \times \mathbf{v}) = (-fv, fu, 0)^T$ , where  $f = 2\Omega \sin(\theta)$  is the Coriolis parameter. On the surface of a sphere with a fixed radius  $r = a$ , the presence of nontrivial metric terms in the local gradient operator  $\nabla = \frac{1}{a}(\sec(\theta) \partial_\varphi, \partial_\theta)^T$  means that the action of the advection operator  $\mathfrak{A}$  on a scalar field  $g = g(\varphi, \theta)$  takes the form

$$\mathfrak{A}(g; \mathbf{u}) \equiv (\mathbf{u} \cdot \nabla) g = \frac{1}{a} \left[ \frac{u}{\cos(\theta)} \partial_\varphi + v \partial_\theta \right] g, \quad (1)$$

while the local horizontal divergence operator  $\mathfrak{D}$  is instead given by

$$\mathfrak{D}(g; \mathbf{u}) \equiv \nabla \cdot (g\mathbf{u}) = \frac{1}{a \cos(\theta)} \left[ \partial_\varphi(gu) + \partial_\theta(\cos(\theta)gv) \right]. \quad (2)$$

For a derivation of these operators, we specifically refer the reader to the discussion leading up to eqs. (20) and (31) in (White, 2003).

## 2.2 Governing Equations

Earth’s weather is predominantly influenced by the dynamics of wind in its atmosphere, which in turn evolves according to the compressible Navier-Stokes momentum equations. Posed in a rotating reference frame, an idealized governing equation can be written in the form

$$\mathbf{v}_t + (\mathbf{v} \cdot \nabla)\mathbf{v} + \mathbf{f} = -\nabla(p/\rho) + \nabla \cdot \boldsymbol{\tau} - \nabla\Phi, \quad (3)$$

where  $p$  denotes the air pressure,  $\rho$  is the air density, and  $\boldsymbol{\tau}$  is the deviatoric stress tensor representing the effects of viscosity. Here, the geopotential  $\Phi$  is defined as a sum of gravitational and centrifugal potential terms via  $\Phi = gr + V_{\text{cen}}$ , where  $-\nabla V_{\text{cen}}(\mathbf{r}) = -\boldsymbol{\Omega} \times (\boldsymbol{\Omega} \times \mathbf{r})$  and  $g$  is the acceleration due to gravity at a given altitude (White, 2003). Many global scale weather models, however, use strategic simplifications of eq. (3) for NWP, omitting, e.g., vertical terms via hydrostatic approximations of the dynamics; again, see White (2003) for a discussion. For reference, we detail an important example of one such ‘primitive equation’ model in the appendix (see eqs. (17) and (18)), which is used in the Integrated Forecast System (IFS) of the European Center for Medium-Range Weather Forecasts (ECMWF, 2021).

## 2.3 The Weak SINDy Algorithm

Given a set of observations  $\mathcal{U} = \{\mathbf{u}(\mathbf{x}_m, t_m)\}_{m=1}^M$  of the state<sup>1</sup>  $\mathbf{u} = (u_1, \dots, u_d)^T$  of a spatiotemporal system, sparse dictionary learning methods for data-driven PDE discovery attempt to equate an evolution operator  $\mathcal{D}^0 \mathbf{u}$  (e.g., a time derivative<sup>2</sup>) with a closed-form expression consisting of functions taken from a matrix-valued library  $\Theta(\mathcal{U})$  of candidate terms  $\{\mathcal{D}^i f_j(\mathbf{u})\}_{i,j=1}^{S,J}$ , evaluated row-wise over each observation  $\mathbf{u}(\mathbf{x}_m, t_m) \in \mathcal{U}$ . Here, each  $\mathcal{D}^i$  denotes one of  $S$  distinct differential operators while each  $f_j$  represents one of  $J$  distinct scalar-valued functions of  $\mathbf{u}$ . In the SINDy algorithm of Brunton et al. (2016), the model discovery problem is recast as a regression problem posed over a sparse set of coefficients  $\mathbf{w} = (w_1, \dots, w_{SJ})$  which weight candidate terms in the library:

$$\text{find sparse } \mathbf{w} \text{ such that: } \mathbf{u}_t(\mathbf{x}_m, t_m) \approx \sum_{i=1}^S \sum_{j=1}^J w(i,j) \mathcal{D}^i f_j(\mathbf{u})(\mathbf{x}_m, t_m), \quad (4)$$

<sup>1</sup> For notational consistency with other work, use ‘ $\mathbf{u}$ ’ here, which need not be a velocity.

<sup>2</sup> Unless stated otherwise, we set the evolution operator  $\mathcal{D}^0$  to  $\partial_t$  to simplify the exposition.

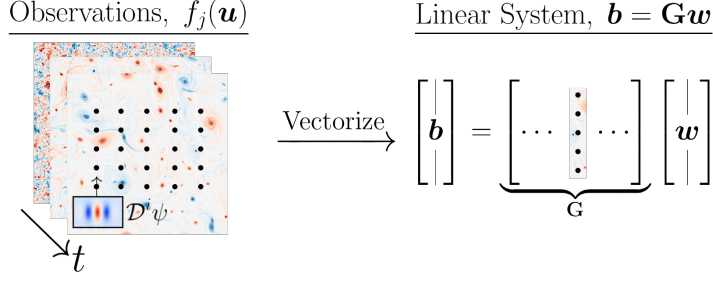


**Figure 1.** A schematic illustrating the construction of the WSINDy linear system of eq. (6). Each column of the weak library  $\mathbf{G}$  represents a strided convolution between a discretized test function derivative  $\mathcal{D}^i \psi$  and a particular function of the data,  $f_j(\mathbf{u})$ . The result is then subsampled over a set of query points  $\{(\mathbf{x}_k, t_k)\}$  (black dots) and vectorized. Here, the data are snapshots of scalar vorticity  $\zeta$  from the numerical simulation of equivalent barotropic turbulence of §5.1.2, made using PyQG (Abernathey et al., 2022) code based upon (McWilliams, 1984).

for each observation  $m = 1, \dots, M$ , where we adopt the notation  $w(i, j) \equiv \mathbf{w}_{(i-1)J+j}$ . The optimal set of coefficients  $\mathbf{w}^*$  are then found by minimizing a regularized loss function  $\mathcal{L}$ , given by

$$\mathbf{w}^* = \underset{\mathbf{w}}{\operatorname{argmin}} \mathcal{L}(\mathbf{w}; \mathbf{u}_t, \Theta), \quad \text{where} \quad \mathcal{L}(\mathbf{x}; \mathbf{b}, \mathbf{A}) \equiv \|\mathbf{b} - \mathbf{A}\mathbf{x}\|_2^2 + \lambda \|\mathbf{x}\|_0. \quad (5)$$

Numerically, we restructure eq. (4) as a linear system  $\mathbf{U}_t = \Theta(\mathbf{U})\mathbf{w}$  by defining  $\mathbf{U} = [\mathbf{u}_1, \dots, \mathbf{u}_d] \in \mathbb{R}^{M \times d}$  as a tensor whose columns are given by vectorizing each component of the data,  $\mathbf{u}_i \equiv \operatorname{vec}\{u_i(\mathbf{x}_m, t_m)\} \in \mathbb{R}^M$ . In turn, we use a library  $\Theta(\mathbf{U}) \in \mathbb{R}^{M \times SJ}$  whose columns are given by  $\Theta(i, j) = \operatorname{vec}\{\mathcal{D}^i f_j(\mathbf{U})\} \in \mathbb{R}^M$  with a corresponding weight vector  $\mathbf{w} \in \mathbb{R}^{SJ \times d}$ . The terms in eq. (4) then take the form of data matrices, schematically represented by

$$\mathbf{U}_t = \begin{bmatrix} | & & | \\ \partial_t \mathbf{u}_1 & \dots & \partial_t \mathbf{u}_d \\ | & & | \end{bmatrix} \quad \text{and} \quad \Theta = \begin{bmatrix} | & & | & & | \\ \mathcal{D}^1 f_1(\mathbf{U}) & \dots & \mathcal{D}^i f_j(\mathbf{U}) & \dots & \mathcal{D}^S f_J(\mathbf{U}) \\ | & & | & & | \end{bmatrix}.$$

The regularization term  $\lambda \|\mathbf{w}\|_0$  in the loss function promotes the selection of a sparse model by penalizing models with a large number of terms, where  $\|\cdot\|_0$  denotes the  $\ell_0$ -“norm.” In practice, this is achieved by using iterative thresholding optimization schemes, which progressively restrict the number of columns of  $\Theta(\mathbf{U})$  available to the model; see Brunton et al. (2016) and Messenger and Bortz (2021).

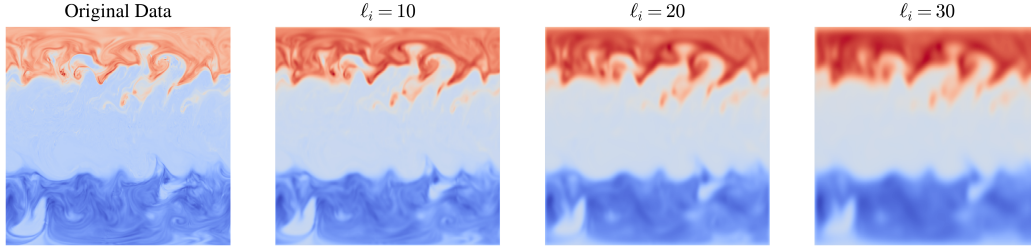


**Figure 2.** Illustrating the effect of increasing the test function support parameter  $\ell$  in the convolution  $\psi * \mathbf{U}$  to select features at increasingly coarsened length scales. The potential vorticity  $\zeta^{\text{PV}}$  from the ERA5 dataset (§3.4) is plotted at  $t = 45$  hr. This and other data in this paper contain modified Copernicus Atmosphere Monitoring Service information [2024].

In the weak formulation of SINDy (Messenger & Bortz, 2021), the linear system in eq. (4) is integrated against a collection  $\{\psi_k\}_{k=1}^K$  of translations of a symmetric, compactly-supported test function  $\psi \in C_c^\infty(\mathcal{X} \times [0, T])$ , where each  $\psi_k = \psi(\mathbf{x}_k - \mathbf{x}, t_k - t)$  is centered at a corresponding *query point*  $(\mathbf{x}_k, t_k)$ . A key benefit of WSINDy is that point-wise derivative computations of the data can be avoided by transferring the differential operators  $\mathcal{D}^i$  from the data  $\mathbf{U}$  to the test functions  $\psi_k$  by repeated integration by parts, exploiting the compact support of the test functions. We note that the sign convention in the argument of each  $\psi_k$  conveniently eliminates the resulting alternating factors of  $-1$  (see Messenger and Bortz (2021) for more details). This integral formulation has been shown to exhibit substantially higher-fidelity results in the presence of noisy data (Messenger & Bortz, 2021). In contrast to eq. (5), the WSINDy weights  $\mathbf{w}^*$  are now found by minimizing a loss function of the flavor  $\mathcal{L}(\mathbf{w}; \mathbf{b}, \mathbf{G})$ ; here,  $\mathbf{b}$  and  $\mathbf{G}$  are, respectively, real-valued  $K \times d$  and  $K \times SJ$  matrices defined by

$$\begin{cases} b_k = (\psi_t * \mathbf{U})(\mathbf{x}_k, t_k), \\ G_k(i, j) = (\mathcal{D}^i \psi * f_j(\mathbf{U}))(\mathbf{x}_k, t_k), \end{cases} \quad (6)$$

where  $*$  denotes the discrete convolution operator, approximated using the trapezoidal rule on a uniformly-spaced discretized grid. The construction of the linear system in eq. (6) is illustrated in Figure 1. We note that this discrete convolution can be efficiently computed via the discrete Fourier transform, although sparse matrix operations may perform better when the support is sufficiently small.

A unique feature of integrating the data against localized test functions  $\psi_k$  is that a particular set of length and time scales can be imposed upon the observed data  $\mathbf{U}$  by choosing a generating test function  $\psi$  with compact support given by

$$\text{supp}(\psi) = [-\ell_{x_1}\Delta x_1, \ell_{x_1}\Delta x_1] \times \cdots \times [-\ell_{x_n}\Delta x_n, \ell_{x_n}\Delta x_n] \times [-\ell_t\Delta t, \ell_t\Delta t], \quad (7)$$

where the  $(n+1)$ -tuple  $\boldsymbol{\ell} = (\ell_{x_1}, \dots, \ell_{x_n}, \ell_t)$  is a tunable hyperparameter and each  $\Delta_i$  represents the spacing of the discretized grid along the  $i^{\text{th}}$ -axis. This allows one to discover effective models for data approximately projected onto the scales  $x_i \approx \ell_{x_i}\Delta x_i$  in space and  $t \approx \ell_t\Delta t$  in time, which is useful for modeling scale-dependent physical mechanisms.<sup>3</sup> Figure 2 illustrates how a progressive coarsening of the weak data  $\psi*\mathbf{U}$  can be achieved by uniformly increasing  $\ell_i$  (here, we use identical  $\ell_i$  for each axis); in this instance, the resulting coarse-grained models become increasingly advection-dominated.

### 2.3.1 Selecting Candidate Terms

When creating a library  $\Theta(\mathbf{U})$  of candidate terms  $\{\mathcal{D}^i f_j(\mathbf{U})\}$ , one can reduce the numerical complexity of the model discovery problem by exclusively including terms of known physical importance; see, e.g., Reinbold et al. (2021). For example, it may be known that the dynamics in a certain context are advection-dominated, prompting the inclusion of material derivatives  $\partial_t + \mathfrak{A}$  as per eq. (1). (In §2.3.2 below, we discuss a strategy for representing library terms that are not integrable-by-parts in a weak form.) In the specific context of fluid dynamics, it can be particularly helpful to consider a conservation perspective, noting that the total transport of a scalar ‘density’  $\rho$  is given by the divergence of its flux  $\mathbf{j}$ ,<sup>4</sup> subject to any forcing  $F$ ,

$$\rho_t = -\nabla \cdot \mathbf{j} + F(\rho, \mathbf{x}, t).$$

An analogous framework for velocities  $\mathbf{u}$  is that of the Euler momentum equation,

$$\mathbf{u}_t + \nabla \cdot (\rho \mathbf{u} \mathbf{u}^T + p \mathbf{I}) = \mathbf{F}(\mathbf{u}, \mathbf{x}, t),$$

where  $p$  represents an effective pressure. Put more concisely, it often makes sense to include candidate terms  $\{\mathcal{D}^i f_j(\mathbf{U})\}$  that are cumulatively capable of representing any known or expected physical sources of flux and forcing.

<sup>3</sup> This notion of ‘scale’ bears a strong resemblance to the same term used in Scale-Space Theory.

<sup>4</sup> For conserved quantities moving in tandem with a background velocity field  $\mathbf{u}$ , the flux is  $\mathbf{j} = \rho \mathbf{u}$ .

In the present setting of atmospheric fluid dynamics, one would like to select a physically motivated library that is capable of parsimoniously representing transport phenomena such as divergence  $\nabla \cdot (\rho \mathbf{u})$ , advection  $(\mathbf{u} \cdot \nabla) \rho$ , horizontal divergence  $(\nabla \cdot \mathbf{u}) \rho$ , diffusion  $\Delta \rho$ , potential gradients  $\nabla \Phi$ , and, e.g., forcing terms  $F$  represented in terms of quadratic monomials.<sup>5</sup> Since the form that the relevant differential operators take depends on the coordinate system in which the original data  $\mathbf{U}$  was measured, we note that a library  $\Theta(\mathbf{U})$  is most useful when it is coordinate-aware. For example, in spherical surface coordinates  $(\varphi, \theta)$  at  $r = a$ , additional metric terms appear in the differential operators, as in eqs. (1) and (2) above.<sup>6</sup> In the numerical experiments of §3.2, we adopt a standardized library to model individual scalar evolution equations  $\partial_t \mathbf{u}_i = \Theta(\mathbf{U}) \mathbf{w}$ , setting

$$\Theta(\mathbf{U}) = \left[ \begin{array}{c|c|c|c|c} | & | & | & | & | \\ \mathbf{1} & \dots & \mathcal{D}^i f_j(\mathbf{U}) & \dots & \mathfrak{D}(\mathbf{u}_i) & \mathfrak{A}(\mathbf{u}_j) \\ | & | & | & | & | \end{array} \right], \quad (8)$$

where for each axis  $d \in \{1, \dots, n\}$  and parameter  $\alpha \in \{0, 1, 2\}$ , we include the corresponding derivative  $\mathcal{D}^i = \partial_{x_d}^\alpha$  with  $i = \alpha + d$ , along with the advection and divergence operators  $\mathfrak{D}$  and  $\mathfrak{A}$ .<sup>7</sup> Moreover, we use a collection of  $J$  functions  $\{f_j\}$  that includes each possible quadratic monomial formed from pairwise components  $\mathbf{u}_k \mathbf{u}_\ell$  of the discretized state variable  $\mathbf{U} = [\mathbf{u}_1, \dots, \mathbf{u}_n]$ , with  $1 \leq k, \ell \leq n$ , so that

$$f_j(\mathbf{u}_1, \dots, \mathbf{u}_n) \in \left\{ \mathbf{u}_1, \mathbf{u}_1^2, \dots, \mathbf{u}_k \mathbf{u}_\ell, \dots, \mathbf{u}_n \mathbf{u}_{n-1}, \mathbf{u}_n^2 \right\}.$$

To discover models posed in terms of spatial derivatives (e.g,  $\mathcal{D}^0 = \partial_x$ ), as we do when discovering compressibility models of the form  $(\nabla \cdot \mathbf{u})_i = \Theta(\mathbf{U}) \mathbf{w}$ , duplicate terms should be removed from the library to prevent the discovery of trivial identities.

### 2.3.2 Augmented Libraries

Here, we present a strategy for creating an *augmented library*  $\Theta'$  that implicitly includes the advection operator  $\mathfrak{A}$ , evaluated on the data, in a weak form. In instances of incompressible flow where  $\nabla \cdot \mathbf{u} = 0$  (e.g., §5.1.2), the divergence operator collapses to the advection operator  $\mathfrak{D}(\rho) = \nabla \cdot (\rho \mathbf{u}) = \mathfrak{A}(\rho) = (\mathbf{u} \cdot \nabla) \rho$ . In these cases, the ad-

<sup>5</sup> WSINDy converges to this class of models in the continuum data limit (Messenger & Bortz, 2024).

<sup>6</sup> Note that the Jacobian determinant in the discrete convolution of eq. (6) becomes  $r^2 \cos(\theta) \Delta \varphi \Delta \theta$ .

<sup>7</sup> For incompressible flows, we have  $\mathfrak{D}(\rho) = \mathfrak{A}(\rho)$ , in which case we do not duplicate the library column.

vection operator can be easily represented by including terms of the form  $(\rho \mathbf{u}_i)_{x_i}$  in the library  $\Theta$ ; e.g., in 2D Cartesian coordinates, we have  $\mathfrak{A}(\rho) = \mathfrak{D}(\rho) = (\rho u)_x + (\rho v)_y$ . However, in more general cases (such as in §3.4 below), some care is needed to represent certain differential operators in a weak form – that is, without resorting to the computation of pointwise derivatives from potentially noisy data. As it turns out, the troublesome terms are those that are not integrable-by-parts.

To begin, we suppose that we have access to horizontal divergence measurements  $\{(\nabla \cdot \mathbf{u})(\mathbf{x}_m, t_m)\}_{m=1}^M$ , as is the case with the assimilated weather data of Section 3.4.<sup>8</sup> Using the product rule for divergence, we consider the expansion  $\mathfrak{A}(\rho) = \mathfrak{D}(\rho) - \mathfrak{C}(\rho)$ , where  $\mathfrak{C}(\rho) \equiv (\nabla \cdot \mathbf{u})\rho$ . As illustrated above for the case of 2D Cartesian coordinates, we assume that the divergence  $\mathfrak{D}$  admits a known expansion in terms of  $N-1$  library columns  $\Theta_{c_1}, \dots, \Theta_{c_{N-1}}$  given by

$$\mathfrak{D}(\mathbf{u}) = \sum_{n=1}^{N-1} \Theta_{c_n} = \sum_{n=1}^{N-1} \mathcal{D}^{i_n} f_{j_n}(\mathbf{U}),$$

where each column index  $c_n \in \{1, \dots, SJ\}$  refers to a corresponding derivative index  $i_n \in \{1, \dots, S\}$  and function index  $j_n \in \{1, \dots, J\}$ . The form of this expansion will depend on the coordinate system being used and the spatial dimension of the system. Similarly, we assume that the horizontal divergence data is given in the  $c_N^{\text{th}}$  library column, with  $\mathfrak{C}(\mathbf{u}) = -\Theta_{c_N}$ . Given the column indices  $c_1, \dots, c_N$ , we then define a corresponding  $SJ \times (SJ+1)$  mask matrix  $\mathbf{M}$  via

$$\mathbf{M} \equiv \begin{bmatrix} \mathbf{I}_{SJ \times SJ} & \boldsymbol{\delta} \end{bmatrix}, \quad \text{where} \quad \delta_i \equiv \begin{cases} 1, & \text{if } i \in \{c_1, \dots, c_N\}, \\ 0, & \text{otherwise.} \end{cases}$$

Right multiplication of  $\mathbf{M}$  against the original library  $\Theta$  yields an augmented library  $\Theta'$  which includes the advection term, that is,  $\Theta' \equiv \Theta \mathbf{M} = [\Theta, \mathfrak{D}(\mathbf{u}) - \mathfrak{C}(\mathbf{u})] = [\Theta, \mathfrak{A}(\mathbf{u})]$ . To arrive at an analogously augmented weak library, we simply define  $\mathbf{G}' \equiv \mathbf{G} \mathbf{M}$ .

Importantly, we note that the technique of library augmentation is not limited to advection operators. In fact, any operator  $\mathbf{A}(\mathbf{u}) \in \text{span}\{\Theta_1, \dots, \Theta_{SJ}\}$  is representable in this manner, although we give the caveat that this process induces collinearity among the corresponding library columns and can result in poor condition numbers  $\kappa(\mathbf{G})$ . To address this issue, we direct the reader to the Appendix (§5.3), where we review a helpful preconditioning approach formulated by Messenger and Bortz (2021).

---

<sup>8</sup> We defer a discussion of more general approaches for future work.

## 2.4 Performance Metrics

To help gauge the quality of the results, we report the coefficient of determination  $R^2$  corresponding to the Weak SINDy regression in Tables 1 and 2, which is defined by

$$R^2 = 1 - \frac{\mathbf{r} \cdot \mathbf{r}}{(\mathbf{b} - \bar{\mathbf{b}}) \cdot (\mathbf{b} - \bar{\mathbf{b}})}, \quad (9)$$

where  $\mathbf{r} \equiv \mathbf{b} - \mathbf{G}\mathbf{w}$  is the residual vector and each entry of  $\bar{\mathbf{b}}$  is the element-wise average of  $\mathbf{b}$ . This metric, which equals the proportion of the variance of the response vector  $\mathbf{b}$  that is explained by the discovered sparse model  $\mathbf{G}\mathbf{w}$ , ranges between 0 and 1, with the values closer to 1 indicating a better performing model. Following Messenger and Bortz (2021), we also report the normalized  $\ell^\infty$  coefficient error  $E_\infty$  whenever the true model and its coefficients  $\mathbf{w}^{\text{true}}$  are known (i.e., in §5.1.2 and §5.1.1), given by

$$E_\infty = \max_j \frac{|\mathbf{w}_j - \mathbf{w}_j^{\text{true}}|}{|\mathbf{w}_j^{\text{true}}|}. \quad (10)$$

The  $E_\infty$  coefficient error represents the max element-wise relative error incurred by the model discovery process. Note that only terms with nonzero coefficients are considered ‘discovered’.

To assess the extent to which the identified models contain the correct terms, we follow (Lagergren et al., 2020; Messenger, Dwyer, & Dukic, 2024) in reporting the *true positive ratio*, defined by

$$\text{TPR} = \frac{\text{TP}}{\text{TP} + \text{FN} + \text{FP}}. \quad (11)$$

Here, TP counts correctly identified terms with non-zero coefficients (i.e., the number of true model terms that were identified), FN counts the terms whose coefficients were falsely identified as zero (the true model terms that have been missed), and FP counts the terms whose coefficients were falsely identified as nonzero (the terms not present in the true model that were selected by the algorithm). Note that a TPR of 1 means that the true model has been discovered in its entirety, and a TPR of 0 means that none of the correct terms were identified.

The PyQG and Dedalus frameworks used in §5.1.2 and §5.1.1, respectively, straightforwardly allow for integration of the discovered WSINDy model forward in time. In these cases, we produce an extrapolated ‘forecast’ dataset  $\mathbf{U}^+$  from the learned model for times  $t > T$  (see Figures 8 and 9). To gauge the predictive power of the learned PDE, we then compare  $\mathbf{U}^+$  to the corresponding output of ground-truth model  $\mathbf{U}^*$  and list the results

in Table 3. To qualify the results, we examine the spatially-averaged relative error at time  $t$ , defined by

$$\bar{\mathcal{E}}(t) \equiv \frac{|\bar{\mathbf{U}}^*(t) - \bar{\mathbf{U}}(t)|}{|\bar{\mathbf{U}}^*(t)|}, \quad \text{where} \quad \bar{\mathbf{U}}(t) \equiv \frac{1}{M} \sum_m \mathbf{U}(\mathbf{x}_m, t_m).$$

The error at the final time of the forecast,  $t = t_F$ , is then defined by  $\bar{\mathcal{E}}_F \equiv \bar{\mathcal{E}}(t_F)$ . Moreover, the reported RMSE is a relative  $L^2$ -error measurement, defined as

$$\text{RMSE} \equiv \frac{\|\mathbf{U}^* - \mathbf{U}\|_{\text{RMS}}}{\|\mathbf{U}^*\|_{\text{RMS}}} = \frac{\|\mathbf{U}^* - \mathbf{U}\|_2}{\|\mathbf{U}^*\|_2}.$$

The time-until-tolerance  $t_{\text{tol}}$  is defined by the first time  $t$  (if such a time exists) such that

$$t_{\text{tol}} \equiv \min_t \{t : \bar{\mathcal{E}}(t) \geq \text{tol}\}, \quad \text{for} \quad \text{tol} = 0.1.$$

In Table 3, the  $R^2$  is defined as in eq. (9), replacing  $\mathbf{r} \mapsto \mathbf{U}^* - \mathbf{U}^+$  and  $\mathbf{b} \mapsto \mathbf{U}^* - \bar{\mathbf{U}}^*$ .

## 2.5 Robustness to Noise

To illustrate the performance of WSINDy in the presence of noisy data  $\mathbf{U} + \boldsymbol{\epsilon}$ , we run repeated numerical experiments on corrupted versions of the ‘Barotropic’ and ‘Spherical’ datasets (the two examples where the true coefficients are known) and report the resulting  $E_\infty$  and TPR averages; see Figure 3, which also displays a  $1\sigma$  confidence interval for the  $E_\infty$  error. Following Messenger and Bortz (2021), we add distinct realizations of artificial i.i.d. noise  $\epsilon_{ij} \in \mathcal{N}(0, \sigma^2)$  in a pointwise fashion to each element of  $\mathbf{U}$ , which we compute by enforcing a variance  $\sigma^2$  satisfying  $\sigma = \sigma_{\text{NR}} \|\mathbf{U}\|_2$  so that  $\sigma_{\text{NR}} = \|\boldsymbol{\epsilon}\|_2 / \|\mathbf{U}\|_2$ , where  $\|\cdot\|_2$  represents the (vectorized)  $\ell^2$  norm. For both examples, we explore noise ratios  $\sigma_{\text{NR}}$  in the range  $0 \leq \sigma_{\text{NR}} \leq 1$  (i.e., up to 100% of the magnitude of the data), generating  $\sim 400$  artificially corrupted datasets by running  $\geq 10$  experiments at each of 40 incremented noise levels  $\sigma_{\text{NR}} \in \{0.025 \cdot j\}_{j=1}^{40}$ . We discuss the results of these experiments in §3.2.

## 3 Numerical Results

We conduct numerical experiments in two contexts of increasing difficulty, using WSINDy to learn equations for simulated (§3.2) and assimilated (§3.4) weather datasets. The assimilated data are produced by fitting high-resolution continuous fields to a sparse set of real weather observations.<sup>9</sup> Results obtained with simulated data provide a sense

<sup>9</sup>In practice, the sparsity of such observations makes data assimilation a ubiquitous procedure in NWP.

of the method’s performance in near-optimal data collection conditions, while numerical experiments performed using assimilated weather data are intended to more closely represent many real-world model discovery applications, where a ‘ground-truth’ model is likely not known.

Beside providing a comparison between results obtained on simulated and assimilated datasets, the examples in §3.2 and §3.4 were specifically chosen to test the ability of Weak SINDy to accurately discover governing equations for data drawn from several common meteorological phenomena: unstable jets in a viscous fluid (§5.1.1), barotropic turbulence (§5.1.2), temperature transport (§5.1.3), and potential vorticity conservation (§3.4). The results of Messenger and Bortz (2021) originally demonstrated that WSINDy can reliably recover several canonical physical mechanisms from noisy data, including “spatiotemporal chaos, nonlinear waves, nonlinear diffusion, shock-forming solutions,” as well as “complex limit cycles.” Our experiments thus aim to complement those of Messenger and Bortz (2021) in the context of atmospheric fluid dynamics.

### 3.1 Implementation Details

Algorithmically, we initialize WSINDy hyperparameters in accordance with the original paper (Messenger & Bortz, 2021), which details methods for selecting test functions with spectral properties matching those in the data and that lead to an implicit filtering of noise. We use a modified sequential thresholding least-squares routine (MSTLS) to compute the model weights  $\mathbf{w}$  by minimizing a loss function of the form of eq. (5), here given in a normalized form by

$$\mathcal{L} = \mathcal{L} \left( \mathbf{w}; \frac{\mathbf{b}_{\text{LS}}}{\|\mathbf{b}_{\text{LS}}\|_2}, \frac{\mathbf{G}}{\|\mathbf{b}_{\text{LS}}\|_2} \right), \quad (12)$$

where  $\mathbf{b}_{\text{LS}} \equiv \mathbf{G}\mathbf{w}_{\text{LS}}$  is the least-squares estimate and where the Lagrange multiplier in eq. (5) is set to  $\lambda = (SJ)^{-1}$  throughout.<sup>10</sup> In each of the results presented below, we use separable test functions  $\psi(\mathbf{x}, t) = \phi_t(t)\prod_{i=1}^n \phi_i(x_i)$  supported on a discrete grid defined by  $\ell$ , as per eq. (7), where each  $\phi_i$  is given by

$$\phi_i(x) = \left[ 1 - \frac{x^2}{(\ell_{x_i} \Delta x)^2} \right]^{p_i} \quad \text{with} \quad p_i = \max \left\{ \left\lceil \frac{\ln(\tau)}{\ln((2\ell_i - 1)/\ell_i^2)} \right\rceil, \bar{\alpha}_i + 1 \right\}.$$

---

<sup>10</sup> Note that Messenger and Bortz (2021) use the notation  $\hat{\lambda}$  to denote the optimal threshold value used in the MSTLS algorithm, which is a distinct quantity from  $\lambda$  as used here.

Dataset	Discovered PDE	$R^2$ (%)	$\mathcal{L}(w)$	$E_\infty$	TPR
Spherical	$h_t = -\nabla \cdot (h\mathbf{u}) - H_0(\nabla \cdot \mathbf{u}),$	100	0.04	$9.1\text{e-}4^*$	$1^*$
	$u_t = -(\mathbf{u} \cdot \nabla)u - fu - g_1\nabla h,$	100	0.08	$7.4\text{e-}4^*$	$1^*$
	$v_t = -(\mathbf{u} \cdot \nabla)v + fu - g_2\nabla h$	100	0.07	$8.0\text{e-}5^*$	$1^*$
	$H_0 = 1.57\text{e-}3, g_1 = 19.96, g_2 = 19.95$				
Barotropic	$\zeta_t = -\nabla \cdot (\zeta\mathbf{u}),$	100	0.02	$3.7\text{e-}3^*$	$1^*$
	$\nabla \cdot \mathbf{u} = 0$	100	0.03	$6.5\text{e-}12$	1
Stratified	$\vartheta_t = -\alpha(\vartheta^2)_x - \beta(\vartheta^2)_y - \gamma\vartheta_y$	96.2	0.17	N/A	N/A
	$\alpha = 2.77, \beta = 2.74, \gamma = 3.30$				

**Table 1.** Model identification results, using metrics defined in §2.4, for the simulated datasets of §3.2 at 0% noise, which are described in detail in the Appendix (§5.1). For readability, each value is rounded to two decimal places, except for the  $R^2$  values, which are rounded to three. The asterisk denotes that a hyperviscosity term was assumed present (see comment in Section 5.1.1)

Here, the parameter  $\tau = 10^{-10}$  is a tolerance indicating the maximum allowable value of the discretized test function  $\psi(\mathbf{x}_m, t_m)$  on boundary of its support, while  $\bar{\alpha}_i$  is the maximum order of derivative taken with respect to  $x_i$  or  $t$ . It is important to emphasize that the chosen test function supports  $\ell$  defines the effective length and time scales that the discovered model governs. Moreover, in each case we use a uniformly-spaced grid of query points  $\{(\mathbf{x}_k, t_k)\}$ . Lastly, to alleviate numerical errors incurred due to high condition numbers  $\kappa(\mathbf{G})$ , we extend the scale-invariant preconditioning method of Messenger and Bortz (2021) to work with data of the form of eq. (8); see the appendix (Section 5) for a description of this approach.

### 3.2 Simulated Data

Referring to Table 1, we observe that the correct models for both the vorticity  $\zeta = \nabla \times \mathbf{u}$  and divergence  $\nabla \cdot \mathbf{u}$  are identified from simulations of highly-turbulent barotropic air flow. Moreover, the right panel of Figure 3 demonstrates that this performance is robust to the presence of high-magnitude i.i.d. noise in the data. Notably, incrementally

increasing the noise ratio  $\sigma_{\text{NR}}$  from 0 to 1 (so that the noise is of equal magnitude to the data,  $\|\boldsymbol{\epsilon}\|_2 = \|\mathbf{U}\|_2$ ) is primarily observed to affect the  $E_\infty$  coefficient error, with the identified PDE very often maintaining the correct selection of terms. In particular, WSINDy recovers the correct form of the vorticity equation (i.e., with  $\text{TPR} = 1$ ) in each trial where  $\sigma_{\text{NR}} \leq 0.825$ . For noise levels  $\sigma_{\text{NR}} > 0.825$ , WSINDy misidentifies spurious diffusion terms in roughly 5% to 10% of the corresponding trials, see the top-right panel of Figure 3.

Interestingly, in the case of the ‘Barotropic’ dataset (§5.1.2), the average  $E_\infty$  coefficient error is *not* initially observed to increase with the noise level  $\sigma_{\text{NR}}$  and instead obtains a local minimum at  $\sigma_{\text{NR}} \approx 0.15$  (see Figure 3, lower-left panel). This phenomenon appears to be related to *stochastic resonance*, in which a more accurate parameter estimate is obtained with a corrupted sample than an uncorrupted sample. Here, we present one possible explanatory theory. First, we note that the sub-grid dissipation (**ssd**) model in eq. (14) is achieved by filtering out the high-frequency content in the spectrum  $\hat{\mathbf{U}}$  of the data  $\mathbf{U}$ ; intuitively, one would expect that the re-introduction of some high-frequency components back into the spectrum when adding noise  $\hat{\mathbf{U}} + \hat{\boldsymbol{\epsilon}}$  to more closely match the spectrum of the unfiltered data (up to a point,  $\sigma_{\text{NR}} < \sigma_{\text{critical}}$ ). Since the unfiltered data represents the non-dissipative model discovered by WSINDy (i.e.,  $\zeta_t = -\nabla \cdot (\zeta \mathbf{u})$  with **ssd** = 0), the parameters would then be more accurately estimated.

Numerical results from the ‘Spherical’ dataset illustrate the application of WSINDy to large-scale geophysical flows in a spherical coordinate system. Given direct measurements of the relevant physical forces, we find that WSINDy correctly identifies the shallow water equations governing a buoyant fluid surface  $h$  and the horizontal velocity  $\mathbf{u}$  on the surface of a sphere, with performance metrics largely mirroring those of the (Cartesian) ‘Barotropic’ dataset.<sup>11</sup> Remarkably, we find that for noise-less data ( $\sigma_{\text{NR}} = 0$ ), Weak SINDy identifies models with coefficients of determination satisfying  $R^2 = 1 + \mathcal{O}(10^{-4})$  for both the ‘Barotropic’ and ‘Spherical’ datasets (see Table 1), indicating that the discovered models explain roughly *all* of the variance of the data.

---

<sup>11</sup> Note that we do not consider the hyperviscosity terms  $\nu \Delta^2(\cdot)$  in §5.1.1, where  $\nu = \mathcal{O}(10^{-9})$ , as true terms in the model, since they are added for numerical stability purposes.

The ‘Stratified’ example (§5.1.3) illustrates the recovery of an effective PDE model that describes the dominant physical mechanisms apparent in the data – in this case, a traveling wave model of the form  $\vartheta_t = -\alpha (\vartheta^2)_x - \beta (\vartheta^2)_y - \gamma \vartheta_y$  (see Table 1). Although in this instance the true form of the coefficients  $\mathbf{w}^{\text{true}}$  are *not* exactly known (see the discussion in §5.1.3), we note that a purely-advective PDE is an especially plausible result, given that the ‘Stratified’ dataset is driven by a constant geostrophic wind  $\mathbf{v}_g$ . We also direct the reader to Figure 6 to show that the identification of this effective transport equation, which describes roughly 96.2% of the variance in the data, is an intuitively plausible result.<sup>12</sup>

### 3.3 Distribution of Residuals

In Figures 3 and 4, we plot component-wise histograms of the WSINDy residual vector  $\mathbf{r} = \mathbf{b} - \mathbf{G}\mathbf{w}^*$ , where  $\mathbf{G}$  and  $\mathbf{b}$  are computed via eq. (6) at 0% noise and  $\mathbf{w}^*$  is computed by applying MSTLS to the loss function  $\mathcal{L}$  defined in eq. (12). Of the four distributions displayed, we note that only that of the ‘Stratified’ dataset (see Figure 3) appears to be normally-distributed, potentially indicating the presence of correlated errors  $\{r_i\}$ . However, the distribution observed in Fig 1 for the ‘Spherical’ dataset of §5.1.1 displays patches of small residuals  $|r_i| = \mathcal{O}(10^{-5})$ , suggesting that the non-normality is incurred by the underlying spatial anisotropy of the data, as illustrated in Figure 9. The more nuanced cases are the distributions corresponding to the ‘Barotropic’ (Table 3, §5.1.2) and ERA5 (Table 4, §5.1.2) datasets, which resemble product distributions (e.g., Bessel-K distributions) arising from the application of ordinary least-squares to an errors-in-variables problem. These examples indicate that an iteratively-reweighted least-squares routine, such as the WENDy algorithm of Bortz et al. (2023), may improve the corresponding parameter estimates. We note that the application of WENDy to the setting of PDEs is currently an area of active research.

---

<sup>12</sup>Rudy et al. (2017) provide an interesting discussion of the discovery of linear versus nonlinear wave equations in the context of interacting solitons in the KdV equation.

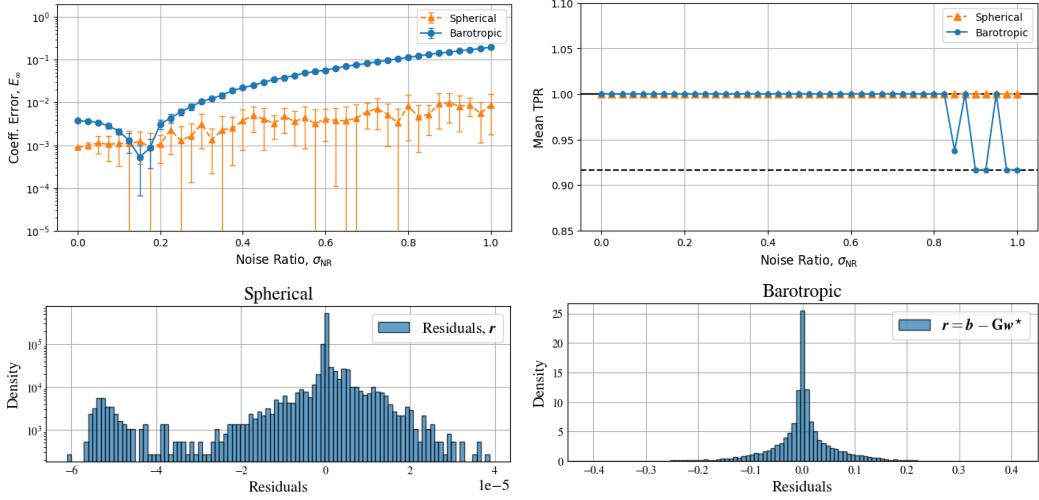


**Figure 3.** Overview of numerical experiments using the ‘Spherical and ‘Barotropic’ datasets, where the true coefficients are known. The top panels illustrate the mean  $E_\infty$  error in a  $1\sigma$  confidence interval (top-left) and TPR (top-right), obtained using at least 10 realizations of Gaussian i.i.d. noise  $\epsilon$  at each noise level  $\sigma_{\text{NR}} \in \{0.025 \cdot j\}_{j=1}^{40}$ . The bottom panels illustrate the distribution of residual values  $\{r_i\}$ , where  $\mathbf{r} = \mathbf{b} - \mathbf{G}\mathbf{w}$ , resulting from solving the linear system defined in eq. (6). Each panel corresponds to a model identification result reported in Table 1 at 0% noise; (top-left) vorticity  $\zeta$  from the ‘Barotropic’ dataset of §5.1.2, (top-right) height  $h$  from the ‘Spherical’ dataset of §5.1.1. See §3.2 and §3.3 for a discussion.

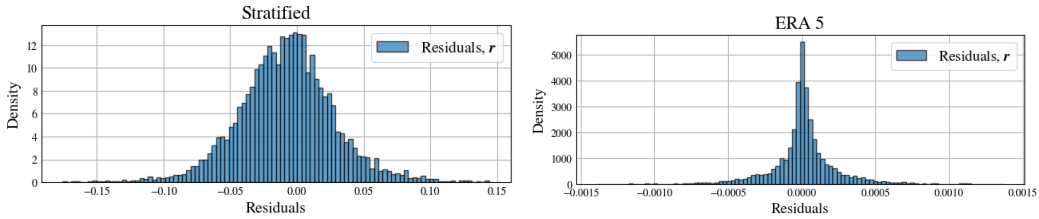


**Figure 4.** Distribution of residuals for the ‘Stratified’ (§5.1.3) and ERA5 (§3.4) datasets, where the true coefficients are not known, complementing Figure 3 above; (center-left) potential temperature  $\vartheta$  from the ‘Stratified’ dataset, (center-right) potential vorticity  $\zeta^{\text{PV}}$  from the ERA5 dataset. See §3.3 for a discussion.

Variable	Discovered PDE	$R^2$ (%)	$\mathcal{L}(w)$
$\zeta^{\text{PV}}$	$\partial_t \zeta^{\text{PV}} = -\alpha(\mathbf{u} \cdot \nabla)\zeta^{\text{PV}} - \beta\tilde{w}\zeta^{\text{PV}}$ $\alpha = 0.70, \beta = 0.29\Omega$	74.4	0.18
$u$	$u_t = -\nabla \cdot (\boldsymbol{\alpha} \odot u\mathbf{u}) - \boldsymbol{\beta} \cdot \nabla u^{\text{ang}} - (\gamma u - \delta \sin(\theta)v)u^{\text{ang}}$ $\boldsymbol{\alpha} = (0.06, 0.04)^T, \boldsymbol{\beta} = (1.56, 0.25)^T, \gamma = 0.07, \delta = 0.41$	23.2	0.64
$v$	$v_t = -\alpha(\mathbf{u} \cdot \nabla)v + \beta u^{\text{ang}}$ $\alpha = 0.21, \beta = 2.37$	30.7	0.36

**Table 2.** Model discovery results for assimilated data (ERA5 dataset) for the assimilated ERA5 datasets of §3.4 (also see §5.1.4), using the same rounding scheme as Table 1 above.

### 3.4 Assimilated Data

We use assimilated weather data<sup>13</sup> from the ECMWF Reanalysis v5 (ERA5), which implements the 4D variational (4D-Var) data assimilation algorithm described by Andersson and Thépaut (2008); see the Appendix (§5.1.4). In 4D-Var, an atmospheric state is estimated from sparse weather data by statistically interpolating between weighted empirical observations and an IFS forecast from an analysis performed 12 hours prior (minimizing a corresponding loss function), which is generated with models similar to eqs. (17) and (18) below. We list our model identification results in Table 2.

A noteworthy result is that, given assimilated weather data, WSINDy recovers a conservation-law-like model governing the evolution of potential vorticity  $\zeta^{\text{PV}}$  in the upper troposphere. The discovery that potential vorticity is conserved in adiabatic air flow is itself regarded as one of the important meteorological results of the 20<sup>th</sup> century (Kooloth et al., 2022). We note that the discovered model, which takes the form  $\partial_t \zeta^{\text{PV}} + \alpha(\mathbf{u} \cdot \nabla)\zeta^{\text{PV}} - \beta\tilde{w}\zeta^{\text{PV}} = 0$  for coefficients  $\alpha \approx 0.7$  and  $\beta \approx 0.29\Omega$ , differs from a true conservation law  $\partial_t \zeta^{\text{PV}} + \alpha(\mathbf{u} \cdot \nabla)\zeta^{\text{PV}} - \beta\tilde{w} \partial_z \zeta^{\text{PV}} = 0$  via the presence of a vertical gradient term  $\tilde{w} \partial_z \zeta^{\text{PV}}$ . This is explained by noting that a single pressure level ( $p = 200$  hPa) was used in the training data, precluding the direct recovery of vertical gradient data  $\partial_z \zeta^{\text{PV}}$  and prompting the inclusion of a correlated term,  $\zeta^{\text{PV}}$ . This phenomenon also il-

<sup>13</sup> Contains modified information from (Copernicus Climate Change Service, 2023).

Dataset	Test Data	RMSE (%)	$R^2$ (%)	$t_{\text{tol}}$	$\bar{\mathcal{E}}_F$ (%)
Spherical ( $h$ )	$[T + \Delta t, T + T/2]$	0.01	100	N/A	0.02
Barotropic ( $\zeta$ )	$[T + \Delta t, T + T/2]$	20.7	95.7	2.5	34.5

**Table 3.** Forecasting accuracy on test data.

illustrates the influence of the query point placement (i.e., the choice of points  $\{(\mathbf{x}_k, t_k)\}$ ), on the model discovery process.

To complement the potential vorticity model, Table 2 also lists the corresponding momentum equations, which were subsequently discovered at the same scales  $\ell$ . While the potential vorticity model explains roughly 74.4% of the variance of the data, the  $u$  and  $v$  models fare substantially worse at 23.2% and 30.7%, respectively. Since the latter models take intuitively plausible forms (cf. eqs. (17) and (18), respectively), this lack of agreement is presumably due to the presence of large latitudinal variations, e.g., the jet streams observed in Figure 7), in the data. We suspect that a nuanced treatment of non-autonomous terms (i.e., varying with  $\theta$ ) in the candidate library would increase the descriptive capacity of the discovered  $u$  and  $v$  models.

### 3.5 Forecasting Accuracy

A striking advantage of symbolic model identification is the ability to perform highly-accurate forecasting whenever the true form of the physics is recovered, which is true even in cases of highly-turbulent data. This phenomena is exemplified by the small forecasting errors reported in Table 3, which demonstrate that a turbulent fluid state can be estimated in a point-by-point manner with an RMS error of only  $\sim 21\%$  for test data extended half the duration of the training data past the final time  $T$ ; see the ‘Barotropic’ results. For data that are less dynamic on the time scales of interest, such as the ‘Spherical’ data, the RMS error is observed to be as small as  $\mathcal{O}(10^{-2})$  over the test interval.

## 4 Conclusion

We have detailed the application of the WSINDy algorithm to atmospheric fluid data, demonstrating that the approach is capable of identifying interpretable PDE models in several illustrative examples of geophysical interest. In particular, WSINDy recov-

ers accurate governing equations for data drawn from turbulent fluid data in both two and three spatial dimensions and in both Euclidean and spherical domains. Since the governing model is learned in a symbolic form, physical phenomena governed by canonical PDEs such as the shallow water equation and the barotropic vorticity equation can be identified directly. Moreover, the weak form representation of the data allows for robust model discovery in the presence of observational noise. We have primarily aimed to demonstrate to the geophysics community that WSINDy represents a powerful tool for data-driven weather modeling.

We conclude with a brief list of natural extensions of this work. In particular, an interesting (and not fully-understood) aspect of using a weak form representation of the dynamics is the ability to investigate a particular range of length and time scales by appropriately localizing the corresponding test functions. We suspect that this is a fruitful direction for future research, potentially bearing upon questions of scale dependence in the setting of data-driven modeling. For example, such work could serve as a foundation for a unified framework capable of smoothly transitioning between weather and climate modeling. Additionally, we suspect that there are interesting applications of weak form model identification in the setting of data assimilation, e.g., using WSINDy for the purpose of discovering physical constraints used in a corresponding loss function.

### **Code and Data Availability**

All code will be publicly available on GitHub at: <https://github.com/MathBioCU/WSINDy4Weather>.

### **Acknowledgments**

The authors would like to thank Ian Grooms (University of Colorado) for guidance regarding weather models and data assimilation. The authors would also like to thank April Tran for insights regarding software development for weak form methods.

This work is supported in part by National Science Foundation grants 2054085 and 2109774, National Institute of Food and Agriculture grant 2019-67014-29919, and Department of Energy grant DE-SC0023346.

## 5 Appendix

### 5.1 Description of Datasets

Our results encompass three distinct numerical simulations, all of which are public available (upon request of the referenced sources):

1. a 2D simulation of equivalent barotropic turbulence<sup>14</sup> with doubly-periodic boundary conditions (see Section 5.1.2), provided by the Python Quasi-Geostrophic (PyQG) project (Abernathy et al., 2022)
2. a simulation of a mid-latitude unstable jet<sup>15</sup> on the surface of a sphere (see Section 5.1.1), provided by the Dedalus project (Burns et al., 2020)
3. a 3D large-eddy simulation of a stably-stratified atmospheric boundary layer<sup>16</sup> in a periodic cube (see Section 5.1.3), provided by the Johns Hopkins Turbulence Database (Li et al., 2008).

#### 5.1.1 Shallow Water Equations on a Sphere (“Spherical”)

This simulation, proposed as a numerical benchmark by Galewsky et al. (2004), models the evolution of an unstable mid-latitude tropospheric jet stream undulating under the influence of a small initial perturbation by solving the viscous shallow-water equations on the surface of a sphere. Using rescaled units in which the radius  $r = 1$ , the equations governing the free surface of the fluid layer  $h$  and the large-scale geophysical flow  $\mathbf{u}$  are given by

$$\left\{ \begin{array}{l} h_t + \nabla \cdot (h\mathbf{u}) = -h_0(\nabla \cdot \mathbf{u}) - \nu\Delta^2 h, \\ \mathbf{u}_t + (\mathbf{u} \cdot \nabla)\mathbf{u} = -\mathbf{f} \times \mathbf{u} - g\nabla h - \nu\Delta^2 \mathbf{u} \end{array} \right. \quad \text{with parameters} \quad \left\{ \begin{array}{l} h_0 = 1.57 \cdot 10^{-3}, \\ \nu = 8.66 \cdot 10^{-9}, \\ g = 19.947, \\ \Omega = 0.263, \end{array} \right. \quad (13)$$

where  $\nabla\mathbf{u}$  denotes the Jacobian matrix of the velocity field  $\mathbf{u}$  and  $\nu\Delta^2$  is the hyperviscosity operator, added for numerical stability. Since the hyperviscosity terms are used for numerical stability, we omit these terms from the vector of true coefficients  $\mathbf{w}^{\text{true}}$  and

<sup>14</sup> <https://pyqg.readthedocs.io/en/latest/examples/barotropic.html>

<sup>15</sup> [https://dedalus-project.readthedocs.io/en/latest/pages/examples/ivp\\_sphere\\_shallow\\_water.html](https://dedalus-project.readthedocs.io/en/latest/pages/examples/ivp_sphere_shallow_water.html)

<sup>16</sup> <https://turbulence.idies.jhu.edu/datasets/geophysicalTurbulence/sabl>

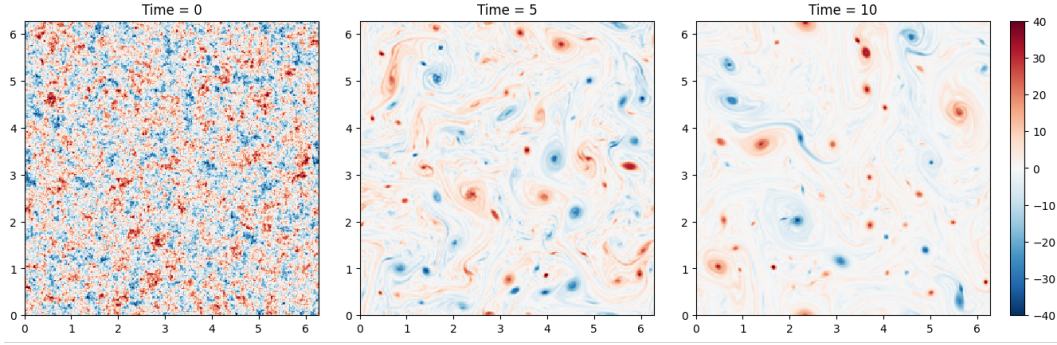


**Figure 5.** Snapshots from a numerical simulation of equivalent barotropic turbulence, made using PyQG (Abernathey et al., 2022) code based upon the turbulence study in (McWilliams, 1984, 1984). The scalar vorticity field  $\zeta$  is plotted. (Color video available online.)

include an asterisk next to the corresponding results in Table 1. A notable benefit of the Dedalus framework is that it is straightforward to write out direct observations of the transport quantities (e.g.,  $\mathfrak{A}$  and  $\mathfrak{D}$ ) during the simulation process. Due to the cumbersome form that these operators take in spherical coordinates, we explicitly include these measurements in the state vector, using:

$$\begin{cases} (h, \mathbf{u}, \mathfrak{D}(h; \mathbf{u}), \mathcal{C}(1; \mathbf{u}), \nu \Delta^2 h), & \text{for the } h_t \text{ model,} \\ (\mathbf{u}, \mathfrak{A}(\mathbf{u}; \mathbf{u}), \mathbf{f} \times \mathbf{u}, \nabla h, \nu \Delta^2 \mathbf{u}), & \text{for the } \mathbf{u}_t \text{ model.} \end{cases}$$

For completeness, we still include  $\mathcal{D}^i f_j$  terms evaluated on  $h$ ,  $u$ , and  $v$  in the weak library  $\mathbf{G}$ , as per eq. (8), which is computed over 3780 query points  $\{(\mathbf{x}_k, t_k)\}$  and contains 61 terms for the  $h_t$  model and 46 for the  $\mathbf{u}_t$  model. In each case, we use support radii  $\ell = (30, 14, 35)$ .

### 5.1.2 Equivalent Barotropic Turbulence (“Barotropic”)

The equivalent barotropic simulation is an idealized model which represents incompressible horizontal wind flow in a regime without temperature gradients or misalignment of pressure and density gradients, which would normally give rise to more complex dynamics. This example uses a special initial condition based on a turbulence study by McWilliams (1984), in which the vorticity field  $\zeta = \zeta(x, y, t)$  is initialized according to a prescribed initial frequency spectrum  $|\hat{\psi}_0| \propto (k[1 + (k/6)^4])^{-1}$  for the stream function  $\psi$  (where  $\zeta = \Delta\psi$ ). This initial condition is chosen because it gives rise to coherent vortex structures (see Fig. 5). Numerically, simulation uses a uniform grid spacing

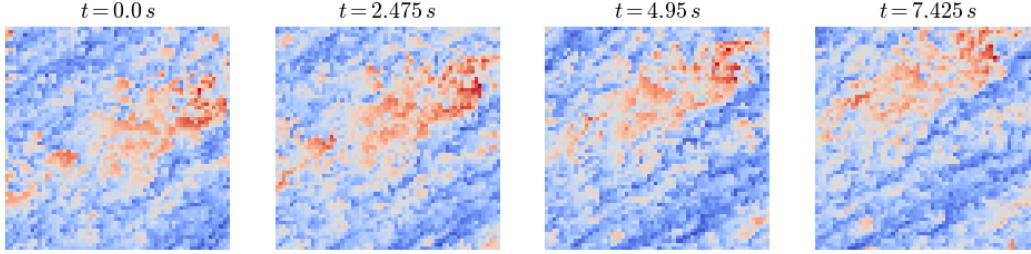


**Figure 6.** Snapshots of the potential temperature field  $\vartheta$  from the ‘Stratified’ dataset (§5.1.3) in the  $(x, y)$  plane at a constant height  $z = 0$ , where warmer colors indicate higher temperatures. The flow is driven by a constant geostrophic wind  $\mathbf{v}_g$  that causes traveling wave dynamics; the corresponding Weak SINDy model is a effective transport equation (see Table 1).

of  $\Delta x = \Delta y = 2\pi/256$  and is integrated for times  $t \in [0, 20]$ . The evolution equation for the vorticity  $\zeta$  is given by the advection equation,

$$\begin{cases} \zeta_t + (\mathbf{u} \cdot \nabla)\zeta = \mathbf{ssd}, \\ \nabla \cdot \mathbf{u} = 0, \end{cases} \quad (14)$$

where  $\mathbf{ssd}$  represents the influence of a “small-scale dissipation” model, which is achieved by implementing a “highly selective spectral exponential filter” term during the integration process (Abernathy et al., 2022). Because this term is difficult to characterize and only affects small wavenumbers, we report results in Table 2 as though  $\mathbf{ssd} = 0$  and include an asterisk (\*) next to the result (cf. the hyperviscosity terms in §5.1.1). We use observations of the scalar fields  $(\zeta, u, v)$  within a 132-term library over 9680 equispaced query points  $\{(\mathbf{x}_k, t_k)\}$ . When discovering models for the compressibility  $\nabla \cdot \mathbf{u}$ , we instead set  $\mathcal{D}^0 = \partial_x$  and use  $(u, v)$  with a 36-term library, discovering equations of the form  $u_x \approx -v_y$ . We set the effective length and time scales by using test function support radii given by  $\ell = (20, 21, 21)$ .

### 5.1.3 Stably-Stratified Atmospheric Boundary Layer Model (“Stratified”)

The final simulated dataset, modeling a stably-stratified atmospheric boundary layer, is sourced from a large-eddy simulation (LES) of the incompressible Boussinesq equations governing wind velocity  $\mathbf{v} = \mathbf{v}(x, y, z, t)$  and potential temperature  $\vartheta = \vartheta(x, y, z, t)$  in a periodic cube given by  $\mathcal{X} = [0, 400]^3$  (meters) for times  $t \in [0, 7.425]$  (seconds). Readers interested in the numerical details are directed towards the recent original work

by McWilliams et al. (2023). Here, we investigate a heavily sub-sampled 2D slice of the spatial domain  $\mathcal{X}$  at a constant height  $z_0 = 0$ , with  $(x, y) \in [0, 62]^2$  subject to a uniform discretization of  $\Delta x = \Delta y = 1$ . The *spatially filtered*<sup>17</sup> potential temperature  $\bar{\vartheta}$  is governed by

$$\bar{\vartheta}_t = -(\bar{\mathbf{v}} \cdot \nabla) \bar{\vartheta} - \nabla \cdot \mathbf{B}, \quad \text{where} \quad \mathbf{B} = \overline{\vartheta \mathbf{v}} - \bar{\vartheta} \bar{\mathbf{v}}, \quad (15)$$

which is coupled to a buoyant momentum model for  $\bar{\mathbf{v}}$  of the form

$$\begin{cases} \bar{\mathbf{v}}_t + (\bar{\mathbf{v}} \cdot \nabla) \bar{\mathbf{v}} = -\mathbf{f} \times (\bar{\mathbf{v}} - \bar{\mathbf{v}}_g) - \nabla \bar{p} + \beta(\vartheta - \vartheta_0) \hat{\mathbf{k}} - \nabla \cdot \boldsymbol{\tau}, \\ \nabla \cdot \bar{\mathbf{v}} = 0 \end{cases} \quad \text{where} \quad \begin{cases} \bar{\mathbf{v}}_g = (8, 0, 0)^T, \\ \theta_0 = 265, \\ \beta = g/\theta_0, \\ \tau_{ij} = \overline{\mathbf{v}_i \mathbf{v}_j} - \bar{\mathbf{v}}_i \bar{\mathbf{v}}_j. \end{cases} \quad (16)$$

In eqs. (15) and (16), the tensors  $\mathbf{B}$  and  $\boldsymbol{\tau}$  represent effective subfilter-scale temperature and momentum models, respectively; since the unfiltered data  $\vartheta$  and  $\mathbf{v}$  are not available, we note that neither  $\mathbf{B}$  nor  $\boldsymbol{\tau}$  can be explicitly constructed. As a consequence, we do not list coefficient errors  $E_2, E_\infty$  for this dataset. We use observations  $(\bar{\vartheta}, \bar{u}, \bar{v}, \nabla \bar{p})$  in 47 and 46-term libraries computed over 4352 query points  $\{(\mathbf{x}_k, t_k)\}$  to discover, respectively, effective evolution equations for  $\bar{\vartheta}_t = \bar{\vartheta}(x, y, t)$  and  $\bar{u}_t = \bar{u}(x, y, t)$  at scales  $\ell = (10, 10, 20)$ .

#### 5.1.4 ERA5 Weather Data

These data represent global-scale hourly snapshots from a single pressure level  $p = 200$  hPa<sup>18</sup> in a domain  $(\varphi, \theta) \in [0^\circ, 360^\circ] \times [-85^\circ, 85^\circ]$ , beginning 00:00 UTC, July 25<sup>th</sup>, 2024 and ending 23:00 UTC, July 28<sup>th</sup>, 2024. We coarsen the original data into longitudinal and latitudinal resolutions of  $\Delta\varphi = \Delta\theta = 1.25^\circ$ , approximate  $r \approx a = 6371$  km, and use the corresponding estimations of the horizontal velocity  $\mathbf{u}$ , horizontal divergence  $(\nabla \cdot \mathbf{u})$ , vertical velocity  $\tilde{w}$ , geopotential  $\Phi$ , and potential vorticity  $\zeta^{\text{PV}}$ . Here, the vertical wind velocity  $\tilde{w} \equiv \dot{\eta}$  is expressed in terms of the pressure-based coordinate  $\eta$  reported by the ECMWF, which opposes the radial wind  $w$ ; see (ECMWF, 2021) for more information. To improve the condition number of the weak library,  $\kappa(\mathbf{G})$ , we manually rescale the potential vorticity data via  $\zeta^{\text{PV}} \mapsto \zeta^{\text{PV}}/\Omega$ . In the model discovery pro-

<sup>17</sup> We denote spatially filtered quantities using overbars  $\overline{(\cdot)}$ .

<sup>18</sup> This pressure level roughly corresponds to the upper Troposphere.

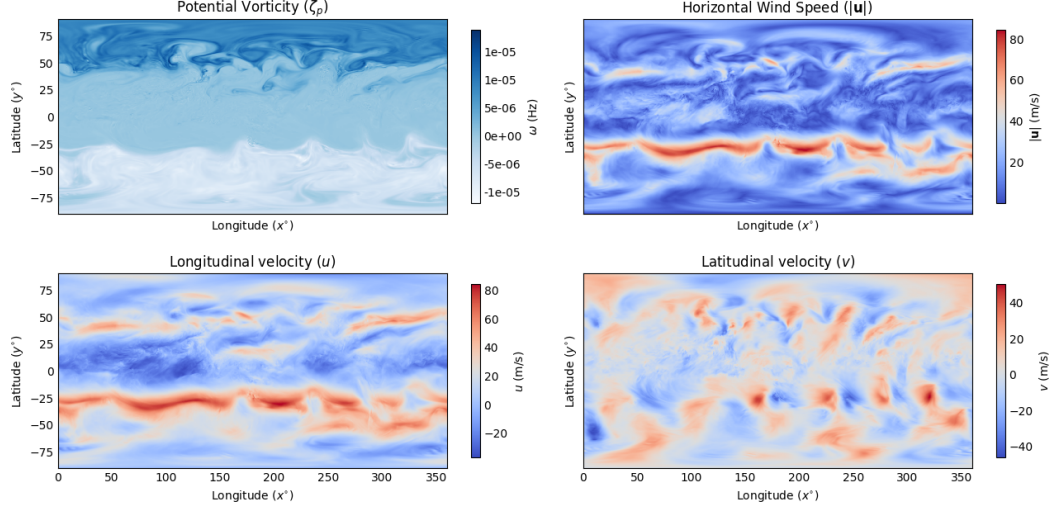


**Figure 7.** A snapshot of global ERA5 data (Copernicus Climate Change Service, 2023), see (§5.1.4), on a single pressure level  $p = 200$  hPa. We use data in the latitudes  $\theta \in [-85^\circ, 85^\circ]$ .

cess, we use observations of the following (linearly-dependent) set of variables:

$$\begin{cases} (\zeta^{\text{PV}}, \frac{1}{a} \tan(\theta) \zeta^{\text{PV}}, u_{\text{ang}}, v, w, \mathcal{C}(1; \mathbf{u})), & \text{for the } \zeta_t^{\text{PV}} \text{ model,} \\ (u, u_{\text{ang}}, v, w, \Phi, \frac{1}{a} \tan(\theta) u, \mathcal{C}(1; \mathbf{u})), & \text{for the } \mathbf{u}_t \text{ model.} \end{cases}$$

where we define the angular velocity  $u_{\text{ang}} \equiv u/(a \cos \theta)$ . When discovering an evolution equation for the potential vorticity,  $\zeta_t^{\text{PV}}$ , we use candidate functions  $\mathcal{D}^i f_j(\mathbf{U})$  given by

$$f_j \in \{1, \zeta, u_{\text{ang}}, v, w, \zeta u_{\text{ang}}, \zeta v, \zeta w, \frac{1}{a} \tan(\theta) \zeta v, \mathcal{C}(\zeta; \mathbf{u})\}, \quad \text{with } \mathcal{D}^i \in \{1, \partial_x, \partial_y\}.$$

Analogously, when discovering a model for  $\mathbf{u}_t$ , we use candidate functions given by

$$f_j \in \{1, u, u_{\text{ang}}, v, w, u \cdot u_{\text{ang}}, u \cdot v, u \cdot w, \frac{1}{a} \tan(\theta) uv, \mathcal{C}(u; \mathbf{u}), \mathcal{C}(v; \mathbf{u}), \Phi\},$$

with  $\mathcal{D}^i \in \{1, \partial_x, \partial_y\}$ .

Here, we compute the results over 4576 query points  $\{(\mathbf{x}_k, t_k)\}$  and use test function supports given by  $\ell = (25, 25, 9)$ . Physically, this choice of  $\ell$  roughly corresponds to a model governing dynamics at length scales of  $30^\circ \times 30^\circ$  latitude and longitude, at a temporal scale of roughly 1 hour.

## 5.2 IFS Primitive Equations

The IFS implements a primitive equation model for the horizontal wind velocity  $\mathbf{u} = (u, v)^T$ ; see (ECMWF, 2021) for a detailed description. For reference, we list a simplified version of the wind model:

$$u_t + \mathfrak{A}(u; \mathbf{u}) - \frac{\tan(\theta)uv}{a} + wu_r - fv + \frac{\Phi_\varphi}{a \cos(\theta)} = \mathcal{P}_u, \quad (17)$$

$$v_t + \mathfrak{A}(v; \mathbf{u}) + \frac{\tan(\theta)u^2}{a} + wv_r + fu + \frac{\Phi_\theta}{a} = \mathcal{P}_v, \quad (18)$$

where  $\mathfrak{A}(\cdot; \mathbf{u}) = (\mathbf{u} \cdot \nabla)(\cdot)$  is the spherical advection operator of eq. (1) with  $r = a$  being the mean radius of the Earth. Here, the  $\mathcal{P}_u$  and  $\mathcal{P}_v$  terms represent additional contributions to the dynamics due to horizontal diffusion and other parameterized physical processes.

## 5.3 Scale-Invariant Preconditioning

Consider a state vector  $\mathbf{u} = (u_1, \dots, u_d) \in \mathbb{R}^d$ , and suppose that the  $\ell^{\text{th}}$  component,  $u_\ell = u_\ell(\mathbf{x}, t)$ , is a scalar field in  $(n+1)$ -dimensions satisfying a PDE given by

$$\mathcal{D}^0 u_\ell = \sum_{i=1}^S \sum_{j=1}^J w_{(i,j)} \mathcal{D}^i f_j(\mathbf{u}), \quad (19)$$

where each  $f_j$  is a homogeneous function of degree  $|\beta^j|$ , given a corresponding multi-index  $\beta^j = (\beta_1^j, \dots, \beta_n^j)$  for each of the fields  $u_1, \dots, u_d$ . Here, we use monomials of the form

$$f_j(\mathbf{u}) = \mathbf{u}^{\beta^j} \equiv u_1^{(\beta_1^j)} \dots u_d^{(\beta_d^j)}.$$

Following the original work in (Messenger & Bortz, 2021, 2021), we introduce a set of rescaled spatial and temporal coordinates via  $(\tilde{x}_1, \dots, \tilde{x}_n, \tilde{t}) = (\gamma_{x_1} x_1, \dots, \gamma_{x_n} x_n, \gamma_t t)$ , with

$$\tilde{u}_\ell(\tilde{\mathbf{x}}, \tilde{t}) = \gamma_{u_\ell} u_\ell \left( \frac{\tilde{x}_1}{\gamma_{x_1}}, \dots, \frac{\tilde{x}_n}{\gamma_{x_n}}, \frac{\tilde{t}}{\gamma_t} \right) = \gamma_{u_\ell} u_\ell(\mathbf{x}, t), \quad \text{for each } \ell = 1, \dots, d.$$

If  $u_\ell$  is a solution to eq. (19) above, then  $\tilde{u}_\ell$  obeys the PDE in the rescaled coordinates,

$$\tilde{\mathcal{D}}^0 \tilde{u}_\ell = \sum_{i=1}^S \sum_{j=1}^J \tilde{w}_{(i,j)} \tilde{\mathcal{D}}^i f_j(\tilde{\mathbf{u}}), \quad (20)$$

where we relate the scaled and original weights ( $\tilde{\mathbf{w}}$  and  $\mathbf{w}$ , respectively) via the change of coordinates

$$\mathbf{w} = \boldsymbol{\mu}^T \tilde{\mathbf{w}}, \quad \text{where } \mu_{(i,j)} = \gamma_{u_\ell}^{(-1)} \left[ \prod_{k=1}^d \gamma_{u_k}^{(\beta_k^j)} \right] \left[ \prod_{r=1}^n \gamma_{x_r}^{(\alpha_r^0 - \alpha_r^i)} \right] \gamma_t^{(\alpha_t^0 - \alpha_t^i)}.$$

The linear system in eq. (6) is then constructed in the rescaled coordinates of eq. (20), where we pick scaling factors  $\gamma_u, \gamma_{\mathbf{x}}, \gamma_t$  such that the condition number of the rescaled library is improved, with  $\kappa(\tilde{\mathbf{G}}) < \kappa(\mathbf{G})$ .

## References

- Abernathy, R., Rochanotes, Ross, A., Jansen, M., Ziwei Li, Poulin, F. J., . . . Tobias (2022, May). *Pyqg/pyqg: V0.7.2*. doi: 10.5281/ZENODO.6563667
- Andersson, E., & Thépaut, J.-N. (2008). ECMWF’s 4D-Var data assimilation system – the genesis and ten years in operations. *ECMWF Newsl.*(115), 8–12. doi: 10.21957/WNMGUIMIHE
- Bortz, D. M., Messenger, D. A., & Dukic, V. (2023). Direct Estimation of Parameters in ODE Models Using WENDy: Weak-form Estimation of Nonlinear Dynamics. *Bull. Math. Biol.*, 85(110). doi: 10.1007/S11538-023-01208-6
- Brunton, S. L., Proctor, J. L., & Kutz, J. N. (2016, April). Discovering governing equations from data by sparse identification of nonlinear dynamical systems. *Proc. Natl. Acad. Sci. U.S.A.*, 113(15), 3932–3937. doi: 10.1073/pnas.1517384113
- Burns, K. J., Vasil, G. M., Oishi, J. S., Lecoanet, D., & Brown, B. P. (2020, April). Dedalus: A flexible framework for numerical simulations with spectral methods. *Phys. Rev. Research*, 2(2), 023068. doi: 10.1103/PhysRevResearch.2.023068
- Charney, J. G., Fjörtoft, R., & Neumann, J. (1950, November). Numerical Integration of the Barotropic Vorticity Equation. *Tellus*, 2(4), 237–254. doi: 10.1111/j.2153-3490.1950.tb00336.x
- Copernicus Climate Change Service. (2023). *ERA5 hourly data on pressure levels from 1940 to present*. [object Object]. doi: 10.24381/CDS.BD0915C6
- ECMWF. (2021, October). IFS Documentation CY47R3 - Part III Dynamics and numerical procedures. In *IFS Documentation CY47R3*. ECMWF.
- Galewsky, J., Scott, R. K., & Polvani, L. M. (2004, January). An initial-value problem for testing numerical models of the global shallow-water equations. *Tellus Dyn. Meteorol. Oceanogr.*, 56(5), 429. doi: 10.3402/tellusa.v56i5.14436
- Gurevich, D. R., Reinbold, P. A. K., & Grigoriev, R. O. (2024). Learning fluid physics from highly turbulent data using sparse physics-informed dis-

- covery of empirical relations (SPIDER). *J. Fluid Mech.*, 996, A25. doi: doi:10.1017/jfm.2024.813
- Karlbauer, M., Maddix, D. C., Ansari, A. F., Han, B., Gupta, G., Wang, Y., ... Mahoney, M. W. (2024, July). *Comparing and Contrasting Deep Learning Weather Prediction Backbones on Navier-Stokes and Atmospheric Dynamics* (No. arXiv:2407.14129). arXiv.
- Kochkov, D., Yuval, J., Langmore, I., Norgaard, P., Smith, J., Mooers, G., ... Hoyer, S. (2024, July). Neural general circulation models for weather and climate. *Nature*. doi: 10.1038/s41586-024-07744-y
- Kooloth, P., Smith, L. M., & Stechmann, S. N. (2022, September). Conservation Laws for Potential Vorticity in a Salty Ocean or Cloudy Atmosphere. *Geophysical Research Letters*, 49(17), e2022GL100009. doi: 10.1029/2022GL100009
- Lagergren, J. H., Nardini, J. T., Lavigne, G. M., Rutter, E. M., & Flores, K. B. (2020, February). Learning partial differential equations for biological transport models from noisy spatio-temporal data. *Proc. R. Soc. A.*, 476(2234), 20190800. doi: 10.1098/rspa.2019.0800
- Lam, R., Sanchez-Gonzalez, A., Willson, M., Wirnsberger, P., Fortunato, M., Alet, F., ... Battaglia, P. (2023, December). Learning skillful medium-range global weather forecasting. *Science*, 382(6677), 1416–1421. doi: 10.1126/science.adi2336
- Li, Y., Perlman, E., Wan, M., Yang, Y., Meneveau, C., Burns, R., ... Eyink, G. (2008, January). A public turbulence database cluster and applications to study Lagrangian evolution of velocity increments in turbulence. *Journal of Turbulence*, 9, N31. doi: 10.1080/14685240802376389
- Lorenz, E. N. (1963, March). Deterministic Nonperiodic Flow. *J. Atmos. Sci.*, 20(2), 130–141. doi: 10.1175/1520-0469(1963)020<0130:DNF>2.0.CO;2
- McWilliams, J. C. (1984, September). The emergence of isolated coherent vortices in turbulent flow. *J. Fluid Mech.*, 146, 21–43. doi: 10.1017/S0022112084001750
- McWilliams, J. C., Meneveau, C., Patton, E. G., & Sullivan, P. P. (2023, July). Stable Boundary Layers and Subfilter-Scale Motions. *Atmosphere*, 14(7), 1107. doi: 10.3390/atmos14071107
- Messenger, D. A., & Bortz, D. M. (2021, October). Weak SINDy For Partial Differential Equations. *J. Comput. Phys.*, 443, 110525. doi: 10.1016/j.jcp.2021

.110525

- Messenger, D. A., & Bortz, D. M. (2024, December). Asymptotic consistency of the WSINDy algorithm in the limit of continuum data. *IMA J. Numer. Anal.* doi: 10.1093/imanum/drae086
- Messenger, D. A., Dwyer, G., & Dukic, V. (2024, December). Weak-form inference for hybrid dynamical systems in ecology. *J. R. Soc. Interface.*, *21*(221), 20240376. doi: 10.1098/rsif.2024.0376
- Messenger, D. A., Tran, A., Dukic, V., & Bortz, D. M. (2024a, September). The Weak Form Is Stronger Than You Think. *arXiv:2409.06751*.
- Messenger, D. A., Tran, A., Dukic, V., & Bortz, D. M. (2024b, October). The Weak Form Is Stronger Than You Think. *SIAM News*, *57*(8).
- Rasp, S., Hoyer, S., Merose, A., Langmore, I., Battaglia, P., Russell, T., ... Sha, F. (2024, June). WeatherBench 2: A Benchmark for the Next Generation of Data-Driven Global Weather Models. *J Adv Model Earth Syst*, *16*(6), e2023MS004019. doi: 10.1029/2023MS004019
- Reinbold, P. A. K., Kageorge, L. M., Schatz, M. F., & Grigoriev, R. O. (2021, December). Robust learning from noisy, incomplete, high-dimensional experimental data via physically constrained symbolic regression. *Nat. Commun.*, *12*(1), 3219. doi: 10.1038/s41467-021-23479-0
- Rudy, S. H., Brunton, S. L., Proctor, J. L., & Kutz, J. N. (2017, April). Data-driven discovery of partial differential equations. *Sci. Adv.*, *3*(4), e1602614. doi: 10.1126/sciadv.1602614
- White, A. A. (2003). Dynamic Meteorology | Primitive Equations. In *Encyclopedia of Atmospheric Sciences* (pp. 694–702). Elsevier. doi: 10.1016/B0-12-227090-8/00139-1
- Zanna, L., & Bolton, T. (2020, September). Data-Driven Equation Discovery of Ocean Mesoscale Closures. *Geophysical Research Letters*, *47*(17), e2020GL088376. doi: 10.1029/2020GL088376

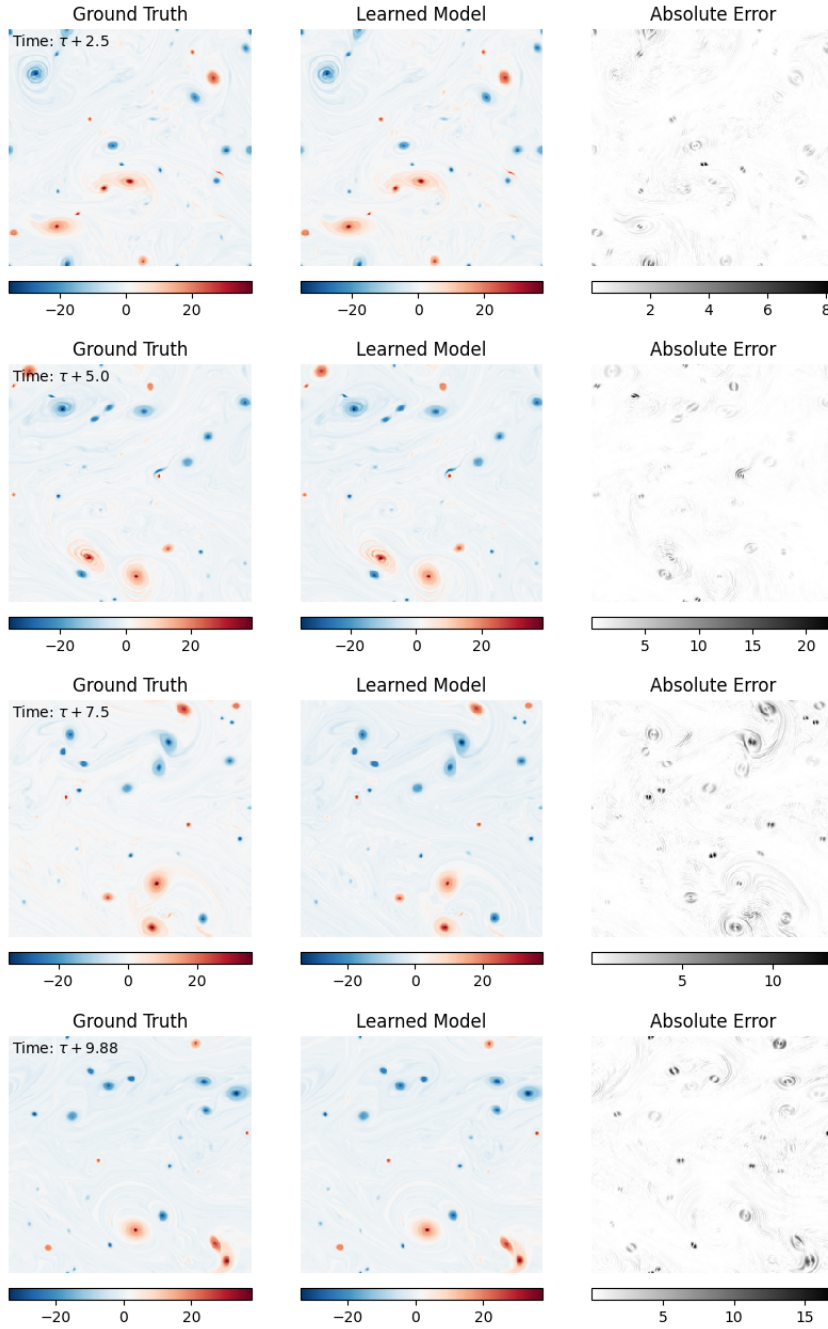


**Figure 8.** Rolling out a forecast for the ‘Barotropic’ dataset for times  $t \in [T, T + 10]$ .

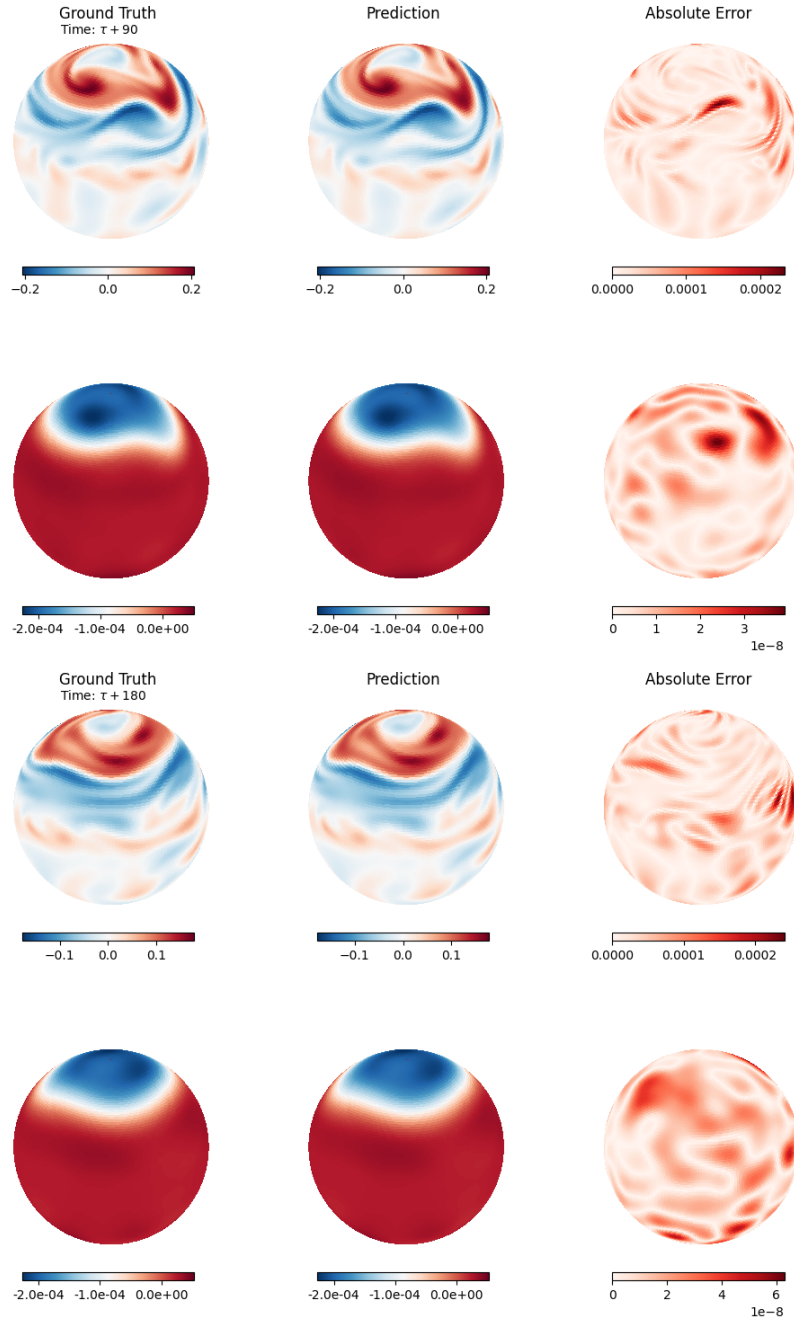


**Figure 9.** Rolling out a forecast for the ‘Spherical’ data for times  $t = 90$  and  $t = 180$ .